Supplementary Materials for

Observational evidence of increasing global radiative forcing

Ryan J. Kramer[1,2,*], Haozhe He[3], Brian J. Soden[3], Lazaros Oreopoulos[1], Gunnar Myhre[4], Piers M. Forster[5], Christopher J. Smith[5,6]

[1]Earth Sciences Division, NASA Goddard Space Flight Center, Greenbelt, MD 20771, USA
[2]Universities Space Research Association, 7178 Columbia Gateway Drive, Columbia, MD 21046, USA
[3]Rosenstiel School of Marine and Atmospheric Science, University of Miami, 4600 Rickenbacker Causeway, Miami, FL 33149, USA
[4]CICERO Center for International Climate and Environmental Research in Oslo, 0318, Oslo, Norway
[5] School of Earth and Environment, University of Leeds, Leeds, LS2 9JT, UK
[6]International Institute for Applied Systems Analysis (IIASA), Laxenburg, 2351, Austria

Corresponding Author: Ryan J. Kramer (ryan.j.kramer@nasa.gov)

Supplemental Appendix:

SA1. Uncertainty Quantification

Following common practice among previous CERES-focused literature (e.g. Loeb et al. 2018a,b), the trend uncertainty quoted throughout the main text is a measure of the linear regression uncertainty, which is largely driven by the internal variability of the timeseries being analyzed. The 95% confidence intervals are given. It is worthwhile to also evaluate uncertainty due to the various assumptions and diagnostic tools that contribute to the estimate of the IRF. As illustrated by equations 7 and 8 in the main text, all-sky IRF is estimated by subtracting radiative-kernel derived, clear-sky radiative responses from the overall clear-sky TOA radiative imbalance (dR^{CS}). This difference, an estimate of the clear-sky IRF (IRF^{CS}) is then divided by a cloud masking constant, Cl, to convert IRF^{CS} into an all-sky IRF. In this supplementary section,

we diagnose uncertainty in IRF trends associated with observations of dR^{CS}, radiative kernels, and Cl. We do so by repeating calculations of the IRF, each time substituting in different values for these terms from different sources as explained below, while keeping all other terms unchanged from the method and data described in the main text. Since the standard trend uncertainty is dependent on these additional sources of uncertainty, it is not practical to combine them to quantify a total, comprehensive measure of uncertainty. We therefore discuss these sources individually, compare their relative magnitude, and summarize the uncertainty budget in Table SA4. We focus on the observational estimate of the IRF.

SA1.1 Uncertainty in dR^{CS}

In this work, observed, total TOA radiative anomalies are diagnosed using radiative flux data from CERES EBAF 4.1. This is identical to CERES EBAF4.0 (Loeb et al. 2018a), except it includes an additional clear-sky radiative flux dataset. While the traditional clear-sky products are comprised only of pixels designated as cloud-free, the new product uses an adjustment factor to mimic a total absence of clouds for all regions, similar to how clear-sky is defined in model simulations (Loeb et al. 2019). While CERES has well documented uncertainty in the magnitude of the TOA radiative flux measurements, our work to estimate the IRF is conducted in anomaly space, where uncertainty in absolute fluxes is irrelevant. Instead, it is the uncertainty due to the stability (or lack thereof) of the observing platform that is important. The presence of spurious trends is frequently assessed by comparing EBAF products to the CERES SSF1deg product, which is considered to be extremely stable (e.g. Loeb et al. 2018a,b). To determine associated uncertainty from stability in the observed timeseries of dR^{CS}, we recompute the IRF using four sources of clear-sky radiative fluxes: CERES EBAF 4.1 assuming clear-skies over the total region, CERES EBAF 4.1 assuming clear-skies over cloud-free regions only (the traditional

method), CERES SSF1deg from Terra and CERES SSF1deg from Aqua. All other components of the IRF calculation are consistent across the four estimates. Linear trends of the global-mean IRF are summarized in Table SA1.

CERES clear-sky Source	Net	LW	SW
EBAF 4.1 – clear-sky (for total region)	0.033	0.027	0.0061
EBAF 4.1 – clear-sky (for cloud-free areas of region)	0.026	0.019	0.0064
SSF1deg Terra	0.027	0.026	0.0015
SSF1deg Aqua	0.024	0.025	-0.0004
Standard Deviation	0.0041	0.0035	0.0034

Table SA1. *Linear trends from 2003 through 2018 in global mean net, longwave (LW) and shortwave (SW) all-sky Instantaneous radiative forcing, estimated with differences observational sources of clear-sky radiative fluxes used to diagnose clear-sky TOA radiative flux anomalies. Units are W/m^2/yr.*

Across the four estimates, we find a standard deviation of $\sigma = 0.0041$ W/m^2/yr for the Net IRF, $\sigma = 0.0035$ W/m^2/yr in the LW and $\sigma = 0.0034$ W/m^2/yr in the SW. We consider this to be an upper bound on uncertainty associated with the stability of the CERES observations, since stability is not the only source of differences between these datasets. Ultimately, we use the new EBAF 4.1 clear-sky fluxes, representing cloud absence over all regions, in the main analysis since it is more consistent with the way clear-sky is defined in radiative kernels, the additional offline radiative transfer calculations of LW GHG IRF, MERRA-2, and in climate models.

S*A1.2 Radiative kernel uncertainty*

Radiative kernels based on CloudSat/CALIPSO observations are used in this study to quantify radiative responses to changes in temperature, water vapor and surface albedo. Radiative kernels are constant in time (beyond a seasonal cycle) and therefore do not contribute to any spurious trends in the diagnosis of the IRF. However, there is uncertainty in the magnitude of the radiative kernels which can contribute to uncertainty in the anomalies and trend of the

IRF. To quantify this, we estimate the IRF using four different sets of radiative kernels: those based on CloudSat/CALIPSO discussed in the main text, as well as radiative kernels derived from the GFDL (Soden et al. 2008), ECHAM6 (Block and Mauritsen 2013) and HadGEM3 (Smith et al. 2020) climate models. All other components of the calculation are consistent across the four estimates. Linear trends of global-mean IRF are summarized in Table SA2.

Radiative Kernel	**Net**	**LW**	**SW**
CloudSat/CALIPSO	0.0333	0.0272	0.0061
GFDL	0.0313	0.0286	0.0027
ECHAM6	0.0320	0.0297	0.0023
HadGEM3	0.0323	0.0263	0.0060
Standard Deviation	0.0008	0.0015	0.0020

Table SA2. *Linear trends from 2003 through 2018 in global mean net, longwave (LW) and shortwave (SW) all-sky Instantaneous radiative forcing, estimated using different sets of radiative kernels. Units are W/m^2/yr.*

We find a standard deviation in trend across the four estimates of $\sigma = 0.0008$ W/m^2/yr for Net IRF, $\sigma = 0.0015$ W/m^2/yr in the LW and $\sigma = 0.0020$ W/m^2/yr in the SW.

SA1.3 Uncertainty in the cloud masking term.

The cloud masking constant, Cl, used to estimate all-sky IRF accounts for the effect of the presence of clouds on the magnitude of the IRF, relative to clear-sky conditions. This quantity is not directly observable and typically requires separate radiative transfer calculations to diagnose. Therefore, like radiative kernels, it contains uncertainty due to radiative transfer error and due to biases in the cloud climatology used in those calculations.

A lack of data prohibits accurately computing the cloud masking directly from observations. All- and clear-sky double-call calculations of the IRF from model simulations offer the best alternative. However, as discussed by Soden et al. (2018), these diagnostics are rarely conducted with model simulations. To the best of our knowledge, none are available for realistic, historical forcing scenarios.

With these limitations, we assume the LW cloud masking is equivalent to the masking of IRF from CO_2 perturbations in this study, which is the dominant GHG driver over the observed period being evaluated. The Coupled Model Intercomparison Project phase 5 (CMIP5, Taylor et al. 2013) includes the necessary double-call calculations from four models to diagnose CO_2 cloud masking, using prescribed sea surface temperature, atmosphere-only simulations where CO_2 concentrations are quadrupled. To diagnose uncertainty in the IRF trends due to Cl, we recompute observed all-sky LW IRF by applying Cl estimated from these four models to the observed clear-sky IRF.

For the SW, there are analogous simulations in CMIP5 (and CMIP6) for aerosol forcing scenarios, but there are no double-call calculations available to diagnose Cl. Instead, we use clear-sky and all-sky Direct Radiative Forcing (DRF) in 15 models included in the AeroCOM Phase II project (Myhre et al. 2013b). Although DRF only includes anthropogenic aerosols, the model-mean Cl from these simulations is 2.70, close to the value from MERRA-2 for SW IRF used in the main text (2.43).

To determine associated uncertainty in IRF trends, we recompute IRF with each LW and SW value of Cl from the model simulations discussed above. Results are summarized in Table SA3.

Model	LW IRF		Model	SW IRF
CanAM4	0.0281		BCC	0.00354
HadGEM2-A	0.0272		CAM4-Oslo	0.00631
INMCM4	0.0253		GEOS_CHEM	0.00627
IPSL-CM5A-LR	0.0243		GISS_MATRIX	0.01081
			GISS-ModelE	0.01024
			GMI	0.00841
			GOCART	0.00913
			HadGEM2	0.00634
			IMPACT-Umich	0.00306
			INCA	0.00726
			ECHAM5-HAM	0.00502
			NCAR-CAM3.5	0.00557
			OsloCTM2	0.00362
			SPRINTARS	0.00290
			TM5	0.00923
Standard Deviation	0.00150		Standard Deviation	0.00253

Table SA3. *Linear trends from 2003 through 2018 in global mean net, longwave (LW) and shortwave (SW) all-sky Instantaneous radiative forcing, estimated using different cloud masking constants derived from 4 CMIP5 models for the LW and 14 AeroCOM models for the SW that provided the radiative flux diagnostics necessary for this calculation.*

The standard deviation across the 4 estimates of LW IRF is $\sigma = 0.00150$ W/m^2/yr and $\sigma =$ 0.00253 W/m^2/yr across the 14 estimates of SW IRF. Since different models are used for the LW and SW component, we estimate the standard deviation of the net IRF ($\sigma = 0.00294$ W/m^2/yr), by summing every possible pair of LW and SW IRF trends listed in Table SA3.

SA1.4 Summary

Table SA4 summarizes the results above and additionally shows the trends and 95% confidence intervals for global-mean IRF as outlined in the main text. The 95% confidence intervals represent roughly ±2 standard errors around the mean. To make the additional measures of uncertainty comparable, the values shown in Table SA4 are doubled from the standard deviations outlined in Tables SA1-3 and are divided by the square root of the number of samples that contributed to each uncertainty calculation (to represent of ± 2 standard errors around the mean)

IRF	Trend	95% Confidence Interval (±)	dR^{CS} uncertainty	Radiative kernel uncertainty	Cloud Mask Uncertainty
Net	0.033	0.007	0.004	0.001	0.0015
LW	0.027	0.006	0.0035	0.0015	0.0015
SW	0.006	0.003	0.0035	0.002	0.0018

Table SA4. *Linear trends and 95% confidence intervals (± value) for observed, global-mean net, longwave (LW) and shortwave (SW) Instantaneous Radiative Forcing diagnosed using the methods and data described in the main text as well as uncertainty (±2 standard errors) from clear-sky TOA radiative anomalies (dR^{CS}), radiative kernels and the cloud masking constant.*

All uncertainties are an order of magnitude smaller than the Net and LW IRF trend and of similar magnitude to the trend in the SW. The IRF trends never cross the zero $W/m^2/yr$ threshold given the sources of uncertainty presented. Therefore, the trends are significantly positive. The largest source of uncertainty is in the linear regression itself, represented by the 95% confidence intervals, followed by uncertainty in dR^{CS}. For the Net IRF, this is arguably to be expected, since the trend from the radiative kernel-derived radiative responses is insignificant.

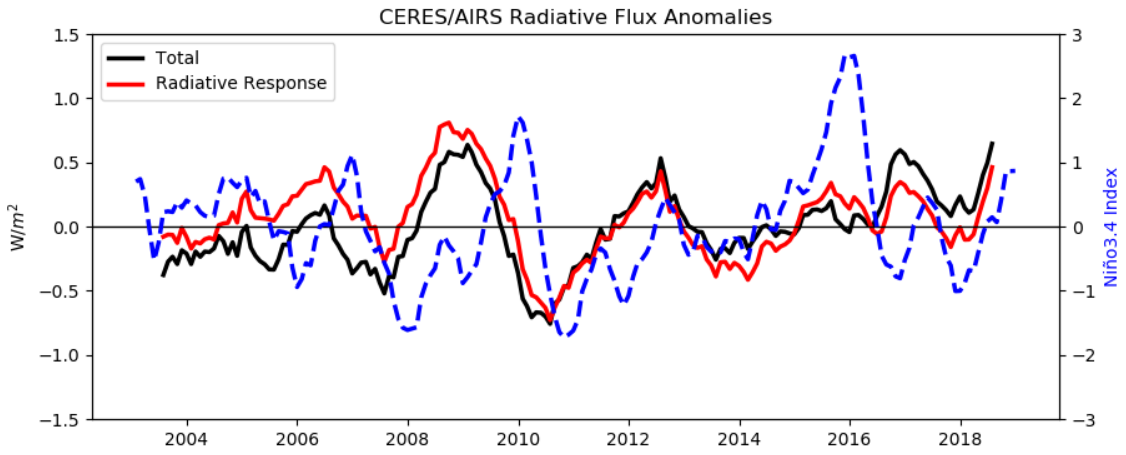

Figure S1. Global-mean total radiative flux anomalies (black) as measured by CERES and the contribution from radiative feedback processes (red). Both quantities are smoothed with a 12-month moving average. The Niño3.4 Index (NOAA/NCEP CPC) is overlaid (blue dashed).

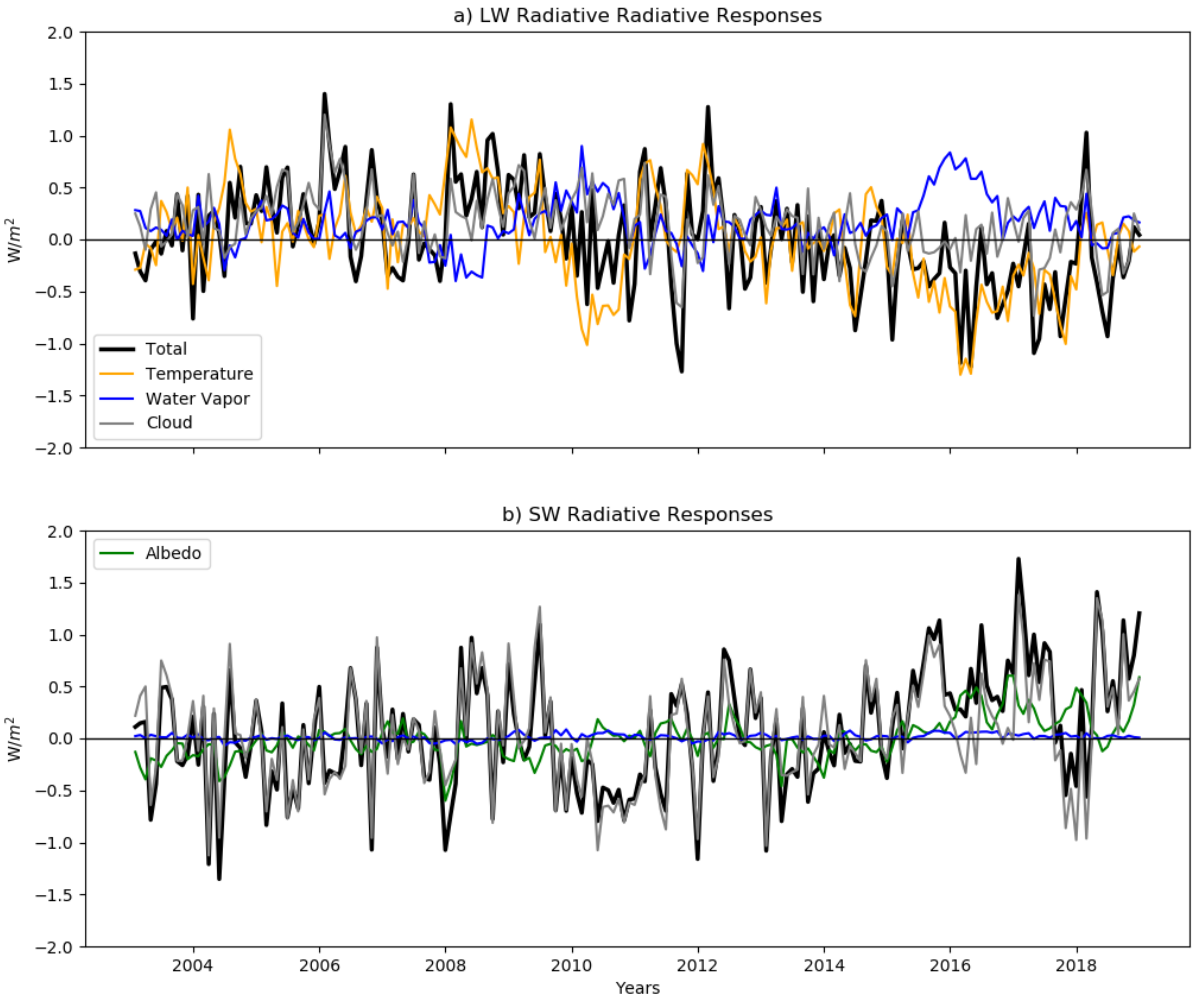

Figure S2. The total a) longwave (LW) and b) shortwave (SW) radiative response and its decomposition into individual radiative responses in CERES/AIRS observations.

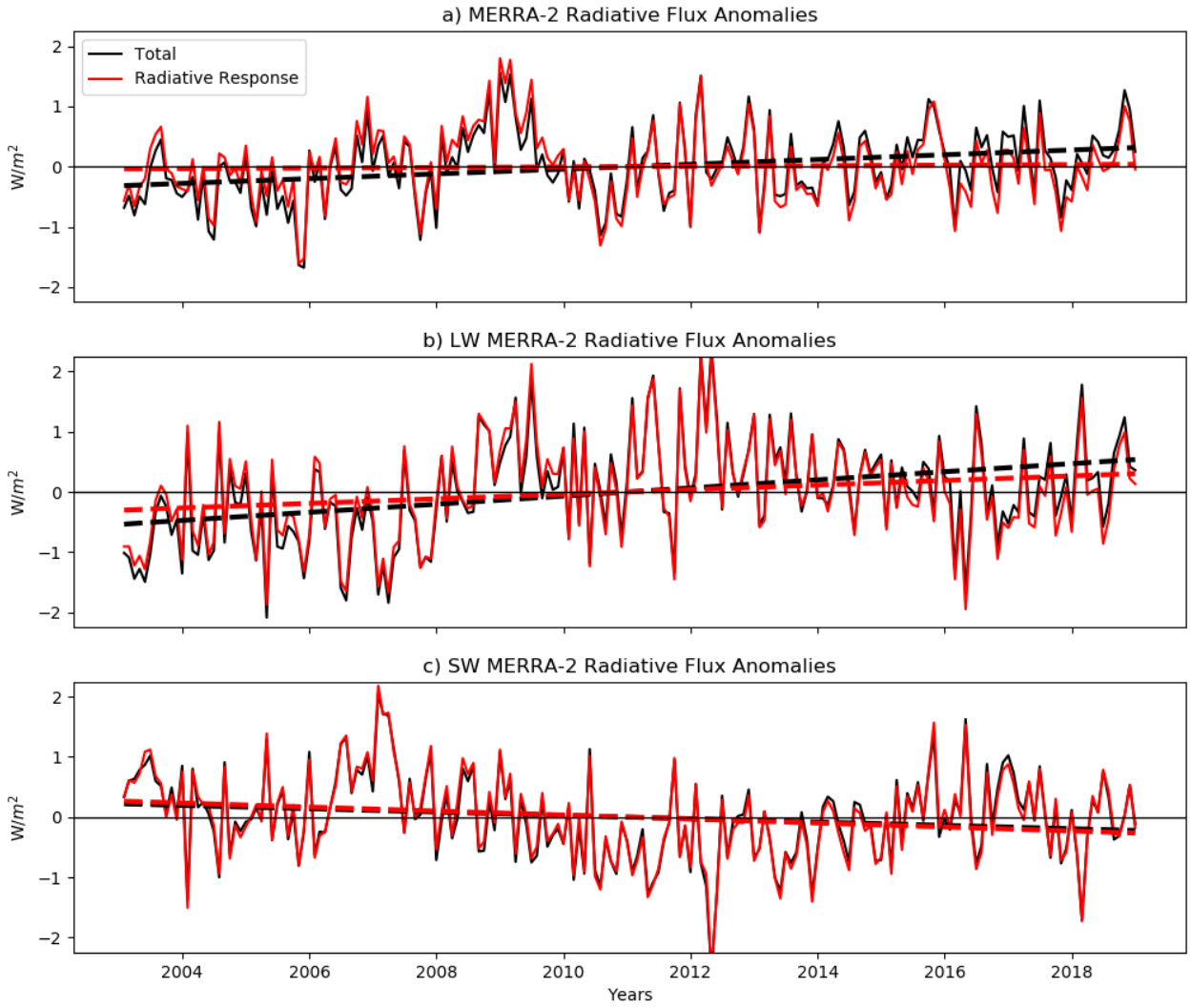

Figure S3. Global-mean, MERRA-2 a) net, b) longwave (LW) and c) shortwave (SW) total radiative flux anomalies (black) from 2003 through 2018 and the contribution to that total from the sum of radiative responses (red). Respective trendlines are displayed as dashed lines.

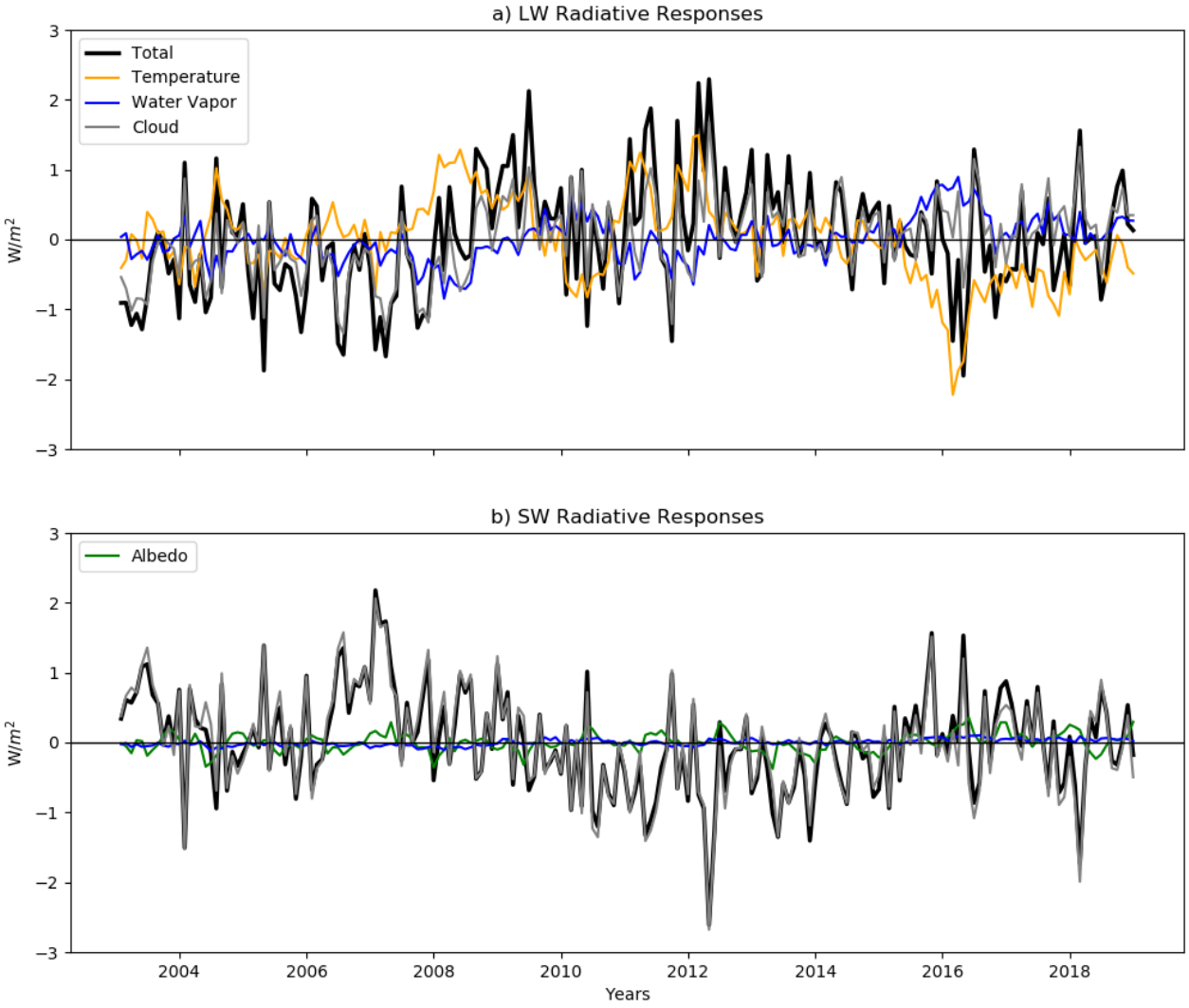

Figure S2. Same as Figure S2 but for MERRA-2.

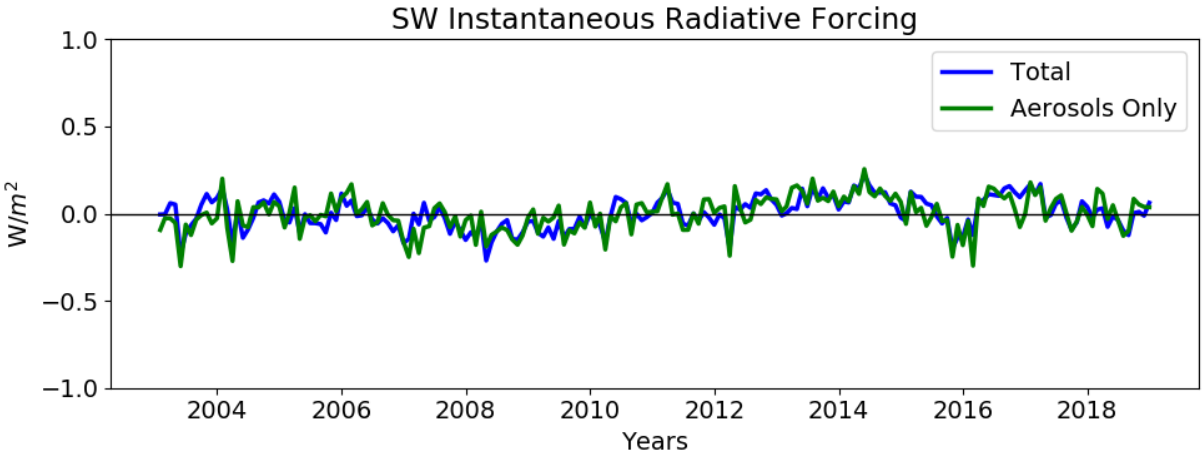

Figure S5. Global-mean a) total shortwave instantaneous radiative forcing (SW IRF) from MERRA-2 derived from the kernel differencing technique and b) aerosol-only SW IRF from direct output of MERRA-2 radiative flux diagnostics.

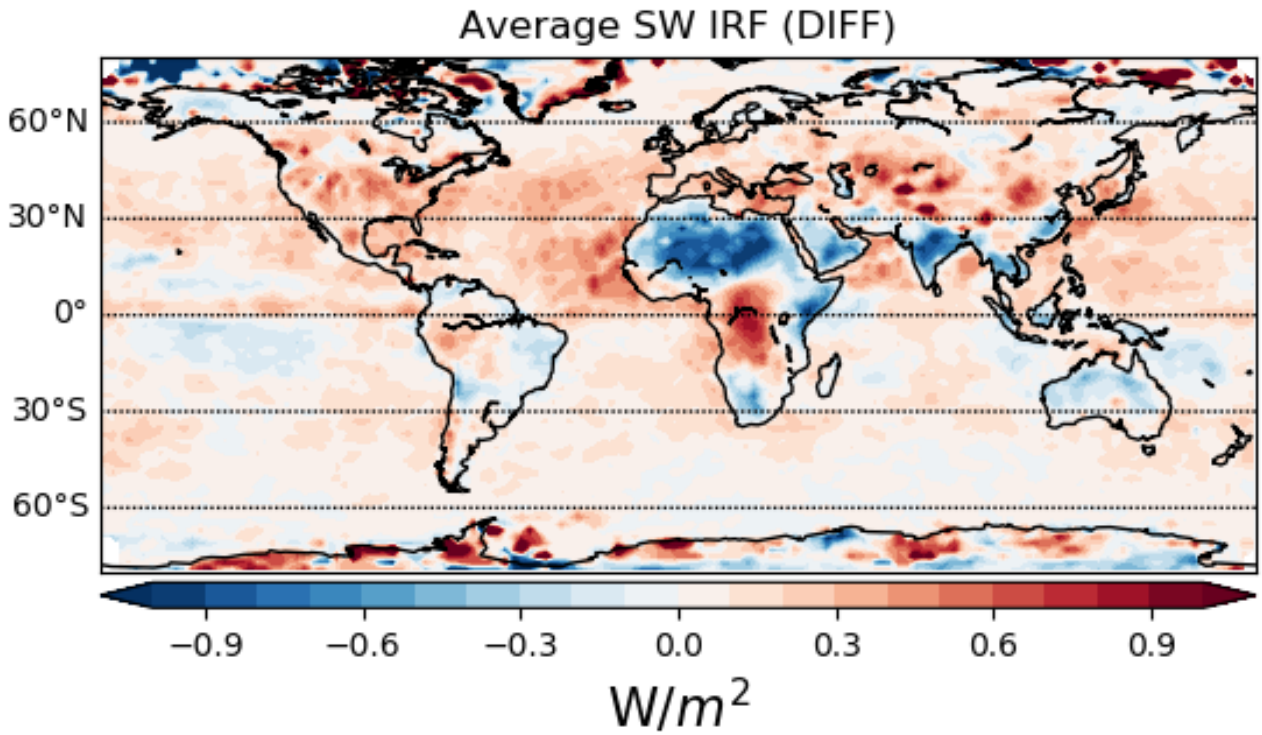

Figure S6. Average difference (CERES/AIRS minus MERRA-2) in SW IRF from 2016 through 2018.

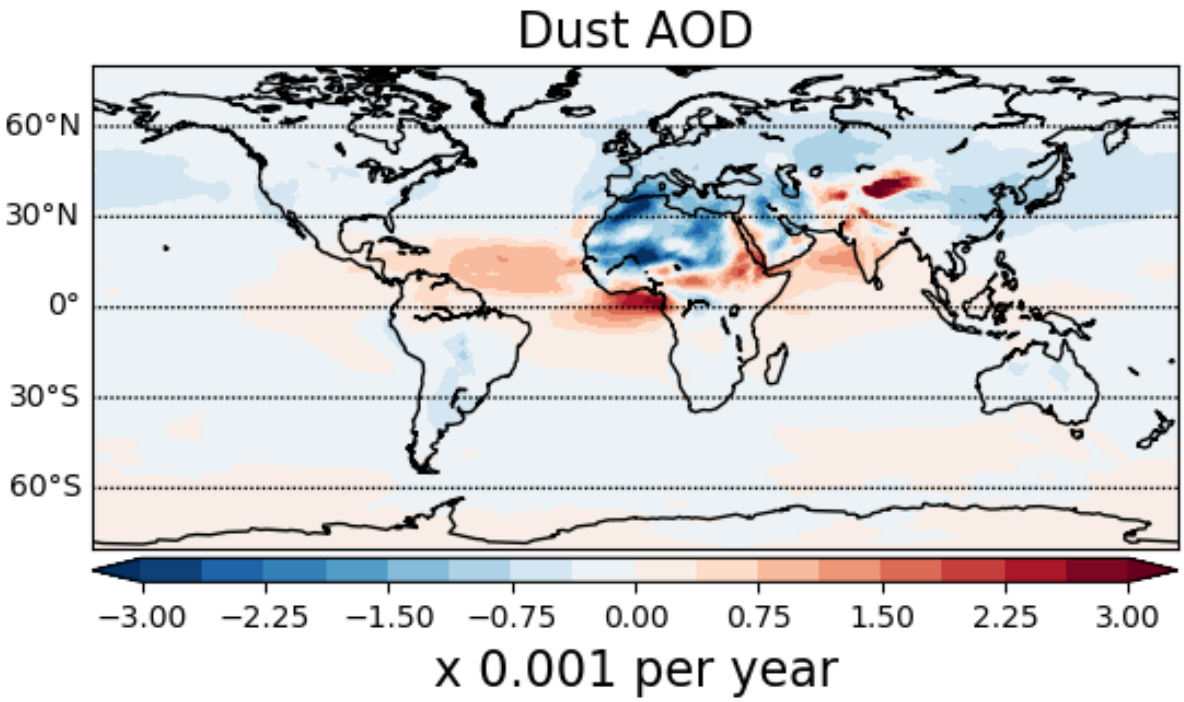

Figure S7. Local linear trends from 2003 through 2018 in dust aerosol optical depth from MERRA-2 reanalysis.

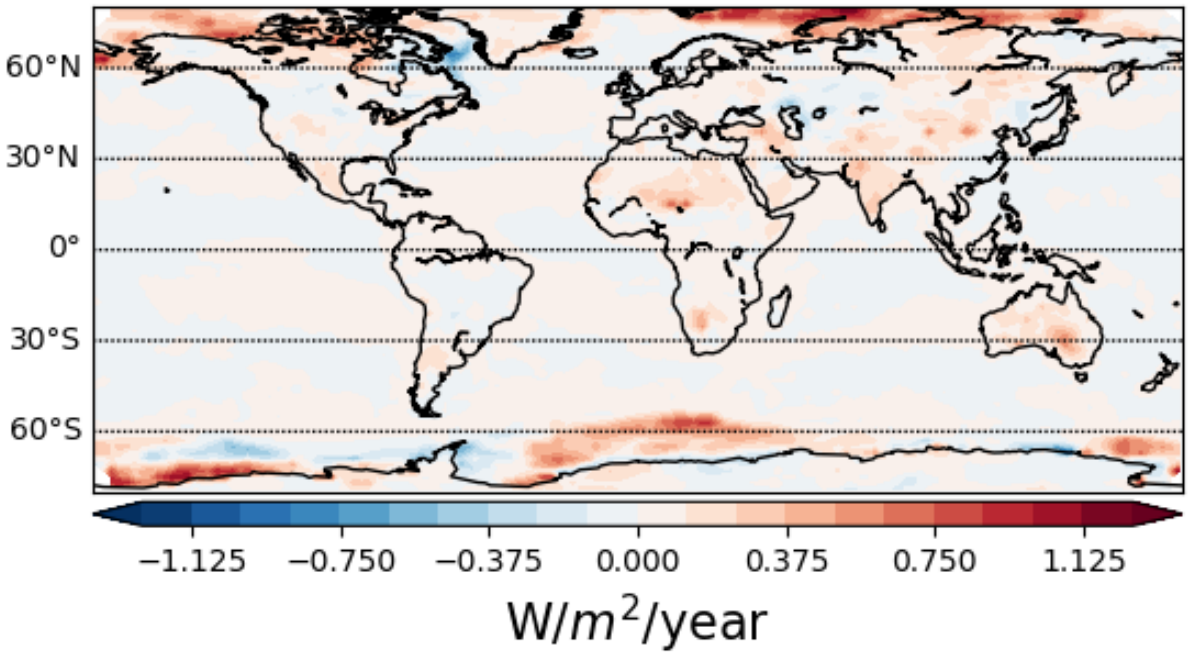

Figure S8. Local linear trends from 2003 through 2018 in clear-sky surface albedo radiative response, used in the kernel differencing method to derive shortwave instantaneous radiative forcing (SW IRF).

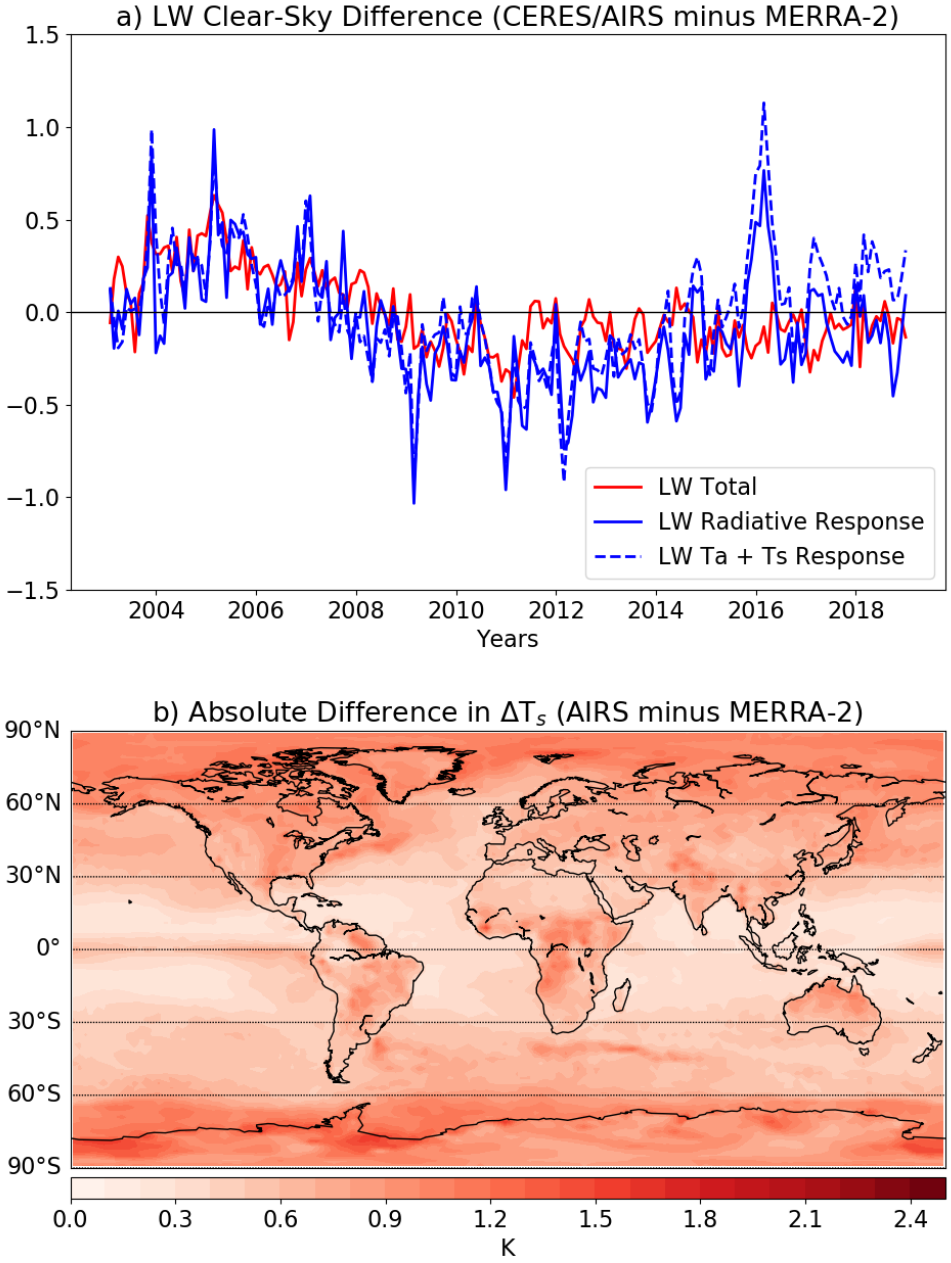

Figure S9. a) Difference between satellite observations and MERRA-2 in global-mean longwave (LW) total radiative flux anomalies (red solid line) as well as the contributions from the sum of LW radiative responses (blue solid) and the LW temperature radiative response (blue dashed), in isolation. b) Mean absolute difference between satellite observations and MERRA-2 in local surface temperature anomalies.

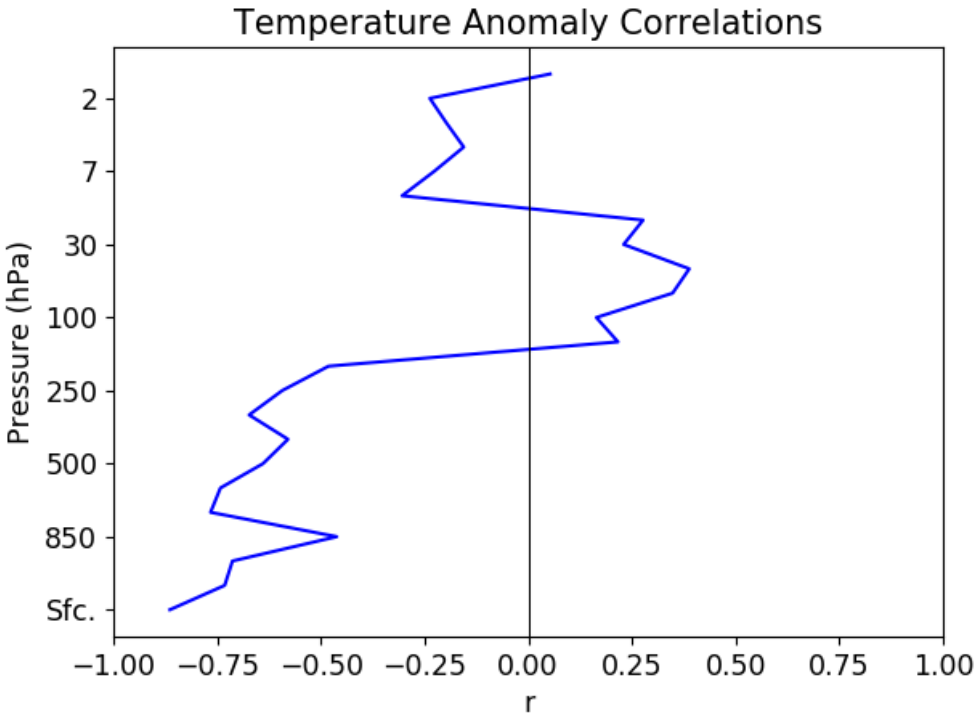

Figure S10. Correlation of the global-mean differences in the temperature feedback between CERES/AIRS and MERRA-2 with differences in temperature anomalies at each vertical level and the surface.

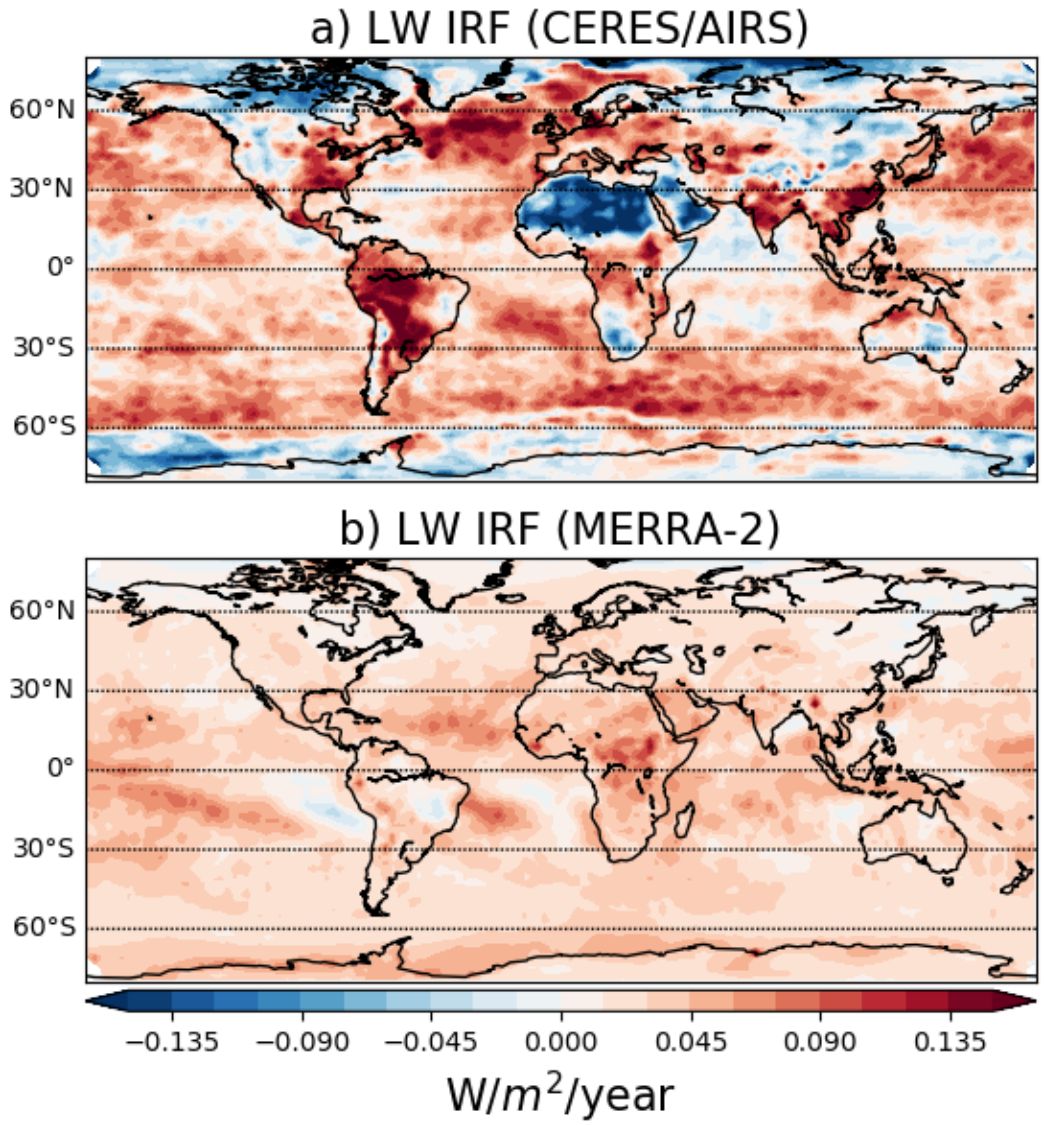

Figure S11. Local linear trends from 2003 through 2018 in all-sky longwave instantaneous radiative forcing (LW IRF) diagnosed in a) CERES/AIRS observations and b) MERRA-2 reanalysis.